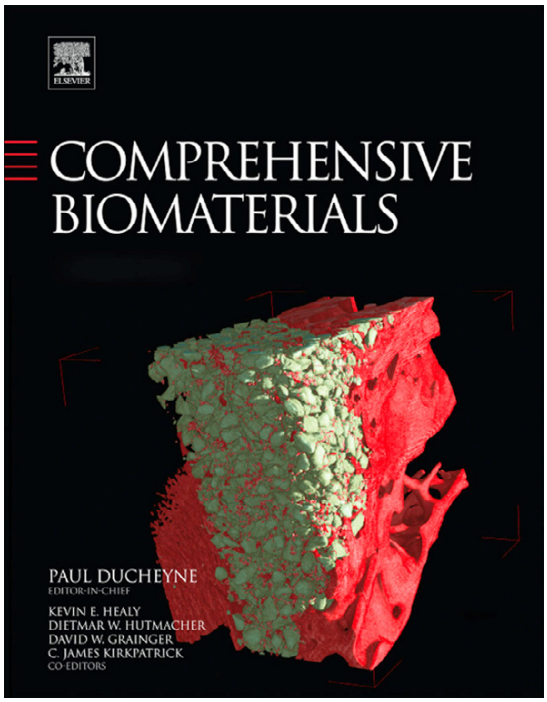




Segers-Nolten I., van Raaij M., and Subramaniam V. (2011) Biophysical Analysis of Amyloid Formation. In: P. Ducheyne, K.E. Healy, D.W. Hutmacher, D.W. Grainger, C.J. Kirkpatrick (eds.) Comprehensive Biomaterials, vol. 2, pp. 347-359 Elsevier.

# 2.219. Biophysical Analysis of Amyloid Formation

**I Segers-Nolten, M van Raaij, and V Subramaniam**, University of Twente, Enschede, The Netherlands





## Glossary

**Amphipathic** Containing polar and nonpolar regions.
**Amyloidosis** Disease resulting from abnormal deposition of amyloid.
**CMC** Critical micelle concentration, minimum phospholipid concentration that forms micelles in water.
**Cross-β conformation** β-sheet secondary protein structure with parallel β-strands oriented perpendicular to the assembly axis.
**Curli** Extracellular bacterial amyloid used for surface adhesion and colony formation.
**Lewy body** Amyloid-containing inclusions found in neurons in the brain of Parkinson's patients.
**Melanosome** Mammalian cellular organelle containing melanin residing in skin and eye cells.
**Micelle** Around 5-nm-diameter spherical aggregate, formed from phospholipids in water above a characteristic concentration, the critical micelle concentration.
**Neurodegenerative disease** Disease characterized by progressive loss of functional neurons in the brain, like Parkinson's and Alzheimer's disease.
**Oligomer** Assembly of a limited number of identical monomers.
**Pme117** A transmembrane protein that mediates the early steps in the formation of melanosomes.
**Polymorphism** The variety of morphologies exhibited by assemblies of identical subunits.
**Protofibril** Intermediate amyloid aggregation state between protofilament and mature fibril.
**Protofilament** Intermediate amyloid aggregation state between monomer and protofibril.
**Raman spectroscopy** Vibrational spectroscopy that yields insight into the secondary structure and chemical composition of a sample by measuring the intensity and spectral distribution of light emitted by a sample after excitation with high-intensity laser light.

## Abbreviations

| | |
|---|---|
| **Aβ** | Amyloid-β |
| **$Aβ_{1-42}$** | Amyloid-β; N-terminal 1–42 residues |
| **AFM** | Atomic force microscopy |
| **CD** | Circular dichroism |
| **CM-AFM** | Contact mode AFM |
| **CMC** | Critical micelle concentration |
| **DNA** | Deoxyribonucleic acid |
| **EPR** | Electron paramagnetic resonance spectroscopy |
| **FRET** | Förster resonance energy transfer |
| **FWHM** | Full width half maximum |
| **HAM** | Hierarchical assembly model |
| **LUV** | Large unilamellar vesicle |
| **MTSL** | 1-Oxy-2,2,5,5 tetramethylpyrroline-3-methyl-methanethiosulfonate |
| **NMR** | Nuclear magnetic resonance |
| **PD** | Parkinson disease |
| **POPG** | 1-Palmitoyl-2-oleoyl-*sn*-glycero-3-(phosphorac-(1-glycerol)) |
| **S129** | Serine residue 129 |
| **SDS** | Sodium dodecyl sulfate |
| **SEM** | Scanning electron microscope |

| | | | |
|---|---|---|---|
| **SM-FRET** | Single-molecule Förster resonance energy transfer | **Triton X-100** | Detergent |
| **STM** | Scanning tunneling microscope | **Trp** | Tryptophan |
| **SUV** | Small unilamellar vesicle | **tTG** | Tissue transglutaminase |
| **ThioT** | Thioflavin T | **UV** | Ultraviolet |
| **TM-AFM** | Tapping mode AFM | | |

**Symbols**

| | | | |
|---|---|---|---|
| $E_{obs}$ | Observed FRET efficiency | $\Theta$ | Ellipticity |

## 2.219.1. Introduction

Insoluble amyloid fibrils self-assemble from a wide variety of proteins that are soluble under physiological conditions. In general, fibrillar amyloid nanostructures have typical diameters of around 10 nm, can grow to several micrometers in length, are extremely stable, and consist mainly of β-sheet folded protein in a typical hydrogen-bonded cross-β conformation (**Chapter 2.204, Peptoids: Synthesis, Characterization, and Nanostructures**). Amyloid formation has long been associated with disease. Besides neurodegenerative disorders, such as Alzheimer's, Parkinson's, Huntington's, and Creutzfeld–Jacob disease, other diseases such as type II diabetes and cardiovascular amyloidosis are also accompanied by the development of amyloid fibrils.[1] Amyloids have also gained more positive recognition since several functional amyloid-containing materials have been identified in nature, from bacteria to humans.[2] Examples are spider silk, biofilms formed from bacterial curli, fibrillar chorion proteins in insect egg shells,[3] and Pme117 fibers in human melanosomes.[4] Amyloid formation also plays an important role in the food industry, where food processing induces fibrillar aggregation of globular proteins, for instance, during heating.[5] In particular, there is a specific interest in the use of amyloid structures for optimization of food texture.

The extreme stability of amyloid fibrils, with a reported mechanical strength similar to polystyrene and nylon, has instigated the interest for use in novel bionanotechnological applications.[6,7] The fibrillar character is particularly interesting for fabrication of nanostructured scaffolds. The spontaneous self-assembly of specific proteins enables the formation of biomaterials with extraordinary characteristics. The proteinaceous nature offers the possibility of using the toolbox of molecular biology to specifically functionalize the fibrils with a variety of chemical or biological conjugation partners resulting in a biomaterial with unique biophysical and physicochemical properties. Compared to chemically synthesized materials, amyloid-based materials have advantageous qualities with respect to biocompatibility and biodegradability. Their versatility offers great potential for creative applications in bionanotechnology. An obvious possibility is the fabrication of nanophotonic or nanoelectronic devices from amyloid-based nanowires.[8,9]

Although protein aggregation in general has been studied extensively for many years, the mechanism of amyloid fibril formation has not been resolved. Full understanding of the assembly mechanism is however essential, not only for development of therapeutic means to fight hitherto incurable diseases but also for optimal utilization of amyloid as nanobiomaterials. To achieve these aims, a range of available biophysical approaches can be deployed that provide molecular level information on the structure of amyloid fibrils.

This chapter gives an overview of biophysical methods that we have applied to the amyloid-forming Parkinson disease (PD) related *α-synuclein* protein,[10,11] but may be considered as relevant for amyloids in general. We describe the revealed information with a focus on those aspects of amyloid formation that are most relevant for a better understanding of the aggregation mechanism, concurrently enhancing insights into the material properties of amyloids. The molecular level assembly process (in this case of α-synuclein) is reflected in characteristics of the monomeric protein and oligomeric folding intermediates, kinetics of fibril formation, fibrillar ultrastructure, and mechanical fibril properties (**Figure 1**).

We describe recent progress in the application of advanced biophysical methods such as (single-molecule) fluorescence spectroscopy, electron paramagnetic resonance (EPR) spectroscopy, circular dichroism (CD) spectroscopy, and atomic force

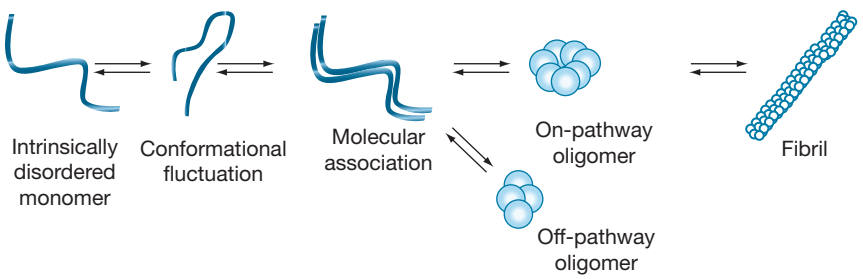


**Figure 1** Schematic representation of the proposed amyloid formation mechanism for human α-synuclein.

microscopy (AFM) to study α-synuclein aggregation. This broad ensemble of approaches provides a deeper perspective into the fascinating research field of amyloids, both from a mechanistic and a materials perspective.

## 2.219.2. Monomer Folding

### 2.219.2.1. α-Synuclein Structural Heterogeneity

It has long been believed that protein stability and function are inevitably associated with proper folding into a characteristic three-dimensional conformation. In recent years, it has become apparent that there exist a large number of intrinsically disordered proteins, such as human α-synuclein, that are functional without having a structured conformation.[12] Both classes of proteins, structured and unstructured, are able to aggregate into amyloid fibrils, requiring partial unfolding of globular proteins or partial acquisition of structure by intrinsically disordered proteins, respectively.[13] The assembly of amyloid fibrils from protein monomers is believed to take place by a nucleation-dependent polymerization process. Partially folded/unfolded monomers may assemble to form oligomers of still unidentified size and conformation, possibly functioning as nuclei, followed by transformation into elongated protofibrillar structures and finally into mature fibrils.[1,14–16]

Human α-synuclein protein (**Figure 2**), a 140 residue intrinsically disordered protein, plays a central role in the etiology of PD,[10] and forms fibrillar aggregates that are found in Lewy bodies in the brain, structures which are the hallmark of the disease.[11,17,18] Three point mutations (A30P, A53T, and E46K) are associated with early onset PD.[19–21] Modifications such as phosphorylation of the serine residue at position 129, and truncations of the protein, are reported to play an important role in the toxicity of α-synuclein.[22–26]

The conformation of the intrinsically disordered protein α-synuclein is known to depend on the environment, binding to targets, and the aggregation state. Although its exact function remains obscure, α-synuclein has been associated with dopamine neurotransmission and regulation of the synaptic vesicular pool.[27] Furthermore, it has been suggested to act at the presynaptic membrane interface.[28] Free in solution, α-synuclein has random-coil-like conformations,[29] but on binding to negatively charged membranes α-helical structures dominate.[30,31] In the fibrillar state, a rigid cross-β structure is prominent,[32] likely lining up the fibril core. Obviously, the protein is structurally highly flexible, which may be fundamental to its putative biological function and implications for disease. The structural transition of the unstructured protein into β-sheet-rich fibrils may be initiated and driven by the occurrence of local structure in α-synuclein molecules. The transient nature, inherent heterogeneity, and low frequencies of occurrence of intramolecular fluctuations and intermolecular associations at physiological concentrations can be addressed only by advanced single-molecule spectroscopy approaches that can detect distributions of structures in ensembles.

Therefore, we and others have used *single-molecule confocal fluorescence microscopy* to study the flexibility and to map the 'structure' of individual α-synuclein monomers, both free in solution and upon binding to SDS (sodium dodecyl sulfate) molecules of monomeric or micellar nature.[33,34] The interaction with SDS is particularly interesting because of its resemblance to membrane components. Single-molecule techniques are specifically required to resolve the occurrence and characteristics of substructures within a population of protein monomers, information that is impossible to obtain from ensemble methods. We have used *single-molecule Förster resonance energy transfer* (SM-FRET) to investigate the structural architecture of α-synuclein.[34] FRET is a nonradiative transfer of the excitation energy from a donor to an acceptor chromophore that involves a distance-dependent interaction between the emission and the absorption transition dipole moments of the donor and acceptor, respectively.[35–37] The rate of energy transfer depends on the spectral overlap of the donor emission and acceptor absorbance, the donor fluorescence quantum yield, the relative orientation of their transition dipole moments, and the distance between donor and acceptor molecules. FRET efficiencies depend on the donor–acceptor separation distance with an inverse sixth power law. The Förster radius, the characteristic distance for a given donor–acceptor pair at which the energy transfer efficiency is 50%, is comparable to the size of biological macromolecules. Therefore, FRET is very useful for measuring distances between different sites on proteins.[38–40]

The N-terminal domain of the α-synuclein protein is known to be involved in membrane binding.[30] Using recombinant techniques, we have engineered a variant of α-synuclein with two cysteines in the putative membrane-binding domain (amino acids 9 and 69). These engineered cysteines act as molecular 'hooks,' and were specifically labeled with donor and acceptor dyes suitable for SM-FRET. FRET efficiency ($E_{obs}$) histograms of 100 pM Alexa Fluor 488 and Alexa Fluor 568 labeled α-synuclein-9C/69C at increasing concentrations of SDS are presented in **Figure 3**. Initially, without SDS, α-synuclein adopts conformations resulting in an $E_{obs}$ centered at 0.54 (first panel, 0 mM, **Figure 3**).

At low SDS concentrations (up to ~0.5 mM), no apparent changes in the histograms were observed. However, upon

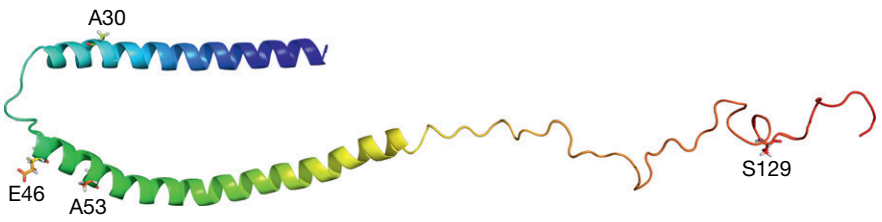


**Figure 2** Representation of the α-synuclein protein indicating the Parkinson's disease-related mutation sites (A30P, E46K, and A53T) and the S129 phosphorylation site.

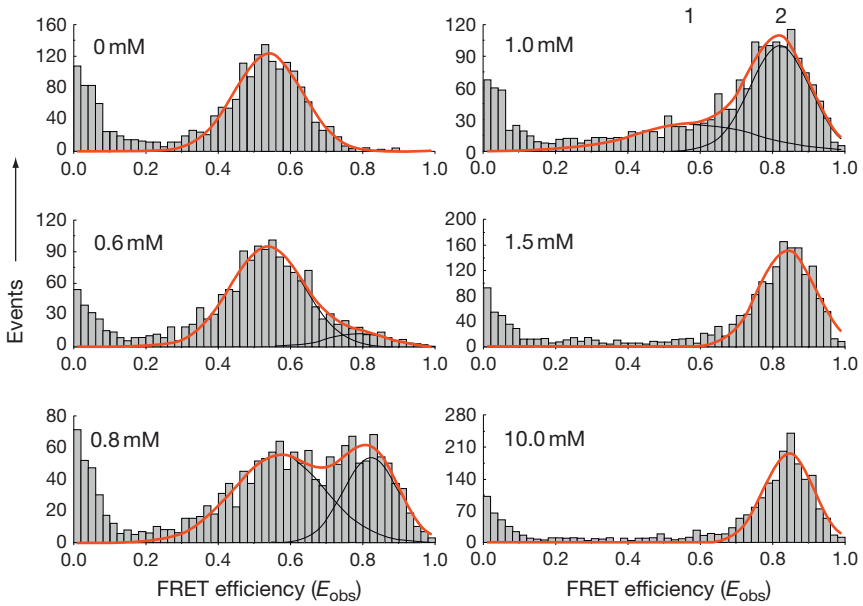


**Figure 3** FRET efficiency histograms of α-synuclein-9C/69C as a function of SDS concentration. Solid lines indicate Gaussian fits to one or two populations (marked 1 and 2). Where applicable, individual Gaussians are shown.

increasing the SDS concentration from 0.5 to 1.0 mM, a clear second distribution centered at $E_{obs}$ ~0.82 and of smaller width appeared (peak 2). The higher $E_{obs}$-value is indicative of a population of proteins where positions 9 and 69 are closer together, leading to increased FRET. The area of the first peak decreased concomitantly with the increase in area of the second peak, suggesting that SDS-induced structural changes in α-synuclein result in one or the other of the conformers, at least within the 1 ms time frame of the experiment. At even higher SDS concentrations (1.5–10.0 mM), the first distribution completely disappeared. Remarkably, above 1.5 mM SDS, although the mean value of the peak did not alter significantly, the width decreased further by ~15% (with an error in the full width half maximum (FWHM) below 5%). We attribute this narrowing of the distribution width to a further stabilization of the horseshoe structure as has been structurally resolved with NMR (nuclear magnetic resonance)[41] (see Figure 4).

We also used *CD spectroscopy* to assess the α-synuclein secondary structure content over the applied SDS concentration range. CD spectroscopy measures directly, without a need for additional labeling, the presence and abundance of specific secondary structures.[42] In CD spectroscopy, the differential absorbance of left- and right-circularly polarized light that is alternately radiated into a sample is detected. A CD spectrum is recorded by measuring this differential absorption as a function of wavelength. CD spectroscopy is mostly performed in the far-UV spectral region, where peptide bonds generate CD signals dependent on the environment. Thus, the CD signals are determined by the secondary structure of the protein and can even be used to semiquantitatively estimate the α-helix, β-sheet, and random-coil content.

CD measurements, with a five orders of magnitude higher protein concentration than that used in the SM-FRET experiments, revealed an increase in α-helix content that corresponded very well with the peak positions and relative areas

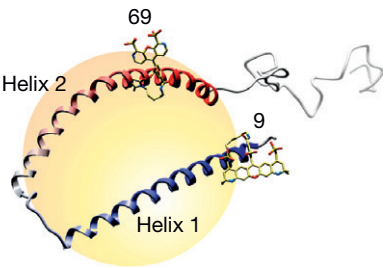


**Figure 4** Representation of the horseshoe conformation of SDS micelle bound AF488 and AF568-labeled α-synuclein-9C/69C. Helix 1 and helix 2 indicate the two putative membrane-binding helices. The unstructured C-terminal tail is also shown.

determined from the FRET efficiency histograms (Figure 5). These data confirm previously reported SDS-induced structural alterations in wild-type α-synuclein.[43]

Taking into account the reported value of 62 Å for the Förster radius of the dye pair used and the mean $E_{obs}$-value at SDS concentrations >1.5 mM, the most frequently found distance between the two dyes in the SDS-bound state can be estimated at 45 Å. This value is higher than the 32 Å distance between amino acid positions 9 and 69 obtained from either NMR[41] or EPR.[44] One should keep in mind, however, that the labels have ~10 Å linkers between the maleimide and fluorophore moiety (Figure 4) and that the observed distance is the distance between the centers of the two fluorophores. As the exact orientation of the dyes with respect to α-synuclein bound to the SDS micelle is not known, it is in this case not possible to translate the observed distance to exact topological distance information within the α-synuclein molecule.

It has been shown that α-synuclein in solution does not behave as a fully random-coil protein; apparently it contains

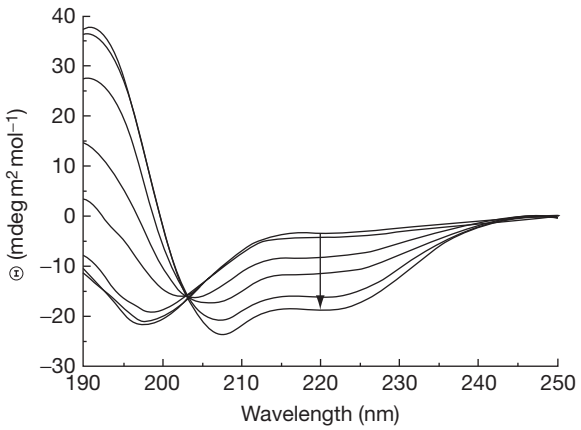


**Figure 5** Structural changes in α-synuclein-9C/69C (unlabeled) induced by increasing concentrations of SDS measured with far-UV circular dichroism. The arrow indicates increasing concentrations of SDS and an increase of α-helix content.

some residual structure in the polypeptide chain.[30,45] The rather wide distributions of the histograms found for free α-synuclein in solution could point to the presence of residual structure within α-synuclein. However, care should be taken in interpreting the distribution widths as they are highly dependent on the timescale of chain motions relative to the observation time of each molecule.[46–50] The apparent broadening (an increase in the FWHM of 35%) of the low FRET peak in the histograms at SDS concentrations up to at least 0.8 mM could point to an increased heterogeneity and/or altered flexibility within this population caused by binding of SDS monomers to the polypeptide chain. However, the broadening could also arise from slower conformer interconversion or chain stiffening caused by SDS binding, especially as the average $E_{obs}$-value did not shift. Although techniques resolving faster timescales will be necessary to elucidate the detailed mechanism, the observed broadening does indicate dynamic structural alterations within α-synuclein, potentially induced by selective SDS binding.

The α-synuclein protein, with its amphipathic motif in the N-terminal region,[29] has been shown to adopt a horseshoe-like structure upon binding to SDS micelles[41] (see **Section 2.219.2.2**) and large unilamellar vesicles (LUVs).[44] Upon closer inspection of our data, we observe that the appearance of peak 2 in SM-FRET occurs just at the onset of α-helix formation measured with CD. This observation is a strong indication that peak 2 contains the conformers with high α-helical content, while peak 1 represents largely unstructured conformers. Furthermore, peak 2 very likely represents the horseshoe conformation,[41] as judged from the high mean $E_{obs}$ and the width corresponding to the state bound to fully formed micelles at much higher SDS concentrations.

The existence of two peaks within the narrow SDS concentration regime (~0.5–1.0 mM) suggests that α-synuclein is able to adopt metastable structures via some sort of all-or-none mechanism for structural rearrangement (on the timescale of the experiment). Even more surprising is that these transitions occur below the CMC (critical micelle concentration) of SDS (6.5 mM at our experimental conditions), as has been reported before.[43] We hypothesize that α-synuclein may locally induce micelle formation at such low amounts that it is not detectable. Interestingly, tryptophan (Trp) residues engineered at positions 9 and 69, probing local polarity, also displayed a dependence on the SDS concentration. However, the blue shifts of the Trp fluorescence approached their maxima already at ~0.6 mM SDS, just at the onset of α-helix formation measured with CD and the appearance of peak 2 in SM-FRET. Thus, below the apparent CMC of SDS, Trps report apolar environments very likely arising from the apolar hydrocarbon tails of SDS, suggesting either micelle formation or at least some sort of SDS encapsulation or binding around the Trp. It is interesting to speculate whether this putative micelle formation is induced by α-synuclein. Once SDS monomers were bound (blue shift) and α-helical structure formation was induced (increase in ellipticity), the second distribution became prominent (SM-FRET). Although analysis of more double-cysteine and single-Trp mutants will be necessary to probe if these transitions occur along the whole peptide, it will also be interesting to resolve whether these apparent sharp transitions also occur *in vivo* and what their role may be.

In conclusion, the SM-FRET approach in combination with ensemble CD and Trp fluorescence spectroscopy has enabled us to discriminate two apparent conformational states of α-synuclein and to analyze these conformers in terms of distribution and heterogeneity, information that is otherwise impossible to extract from ensemble measurements.

### 2.219.2.2. Antiparallel Arrangement of α-Synuclein Helices

The mode of binding of α-synuclein to membranes has generated significant discussion in the literature. It was proposed that α-synuclein binds to membranes either as an extended, continuous helix (residues 1–100)[51–53] or in a horseshoe-like conformation, consisting of helix 1 (residues 3–37), a bend around residue 42, and helix 2 (residues 45–92),[41] with the two helices in an antiparallel arrangement but not touching (see **Figure 4**).[54,55] Supporting evidence for the latter proposal was given by the single-molecule fluorescence study described in the previous paragraph, revealing structural information from interaction of α-synuclein with monomeric and micellar SDS. Micelles have typical diameters[56] of 5 nm and may thus be too small to accommodate α-synuclein in the extended conformation (around 15 nm for an extended helix of 100 residues).[57] Therefore, micelles could enforce an antiparallel configuration of the helices even if that is not the preferred state of α-synuclein on a larger surface such as that of a biological membrane. In contrast, even small unilamellar vesicles (SUVs) have diameters on the order of 20–30 nm,[30] providing a surface area that is large compared to the dimensions of α-synuclein[57] and a larger radius of curvature than that of micelles. Therefore, SUVs are more suitable models for biological membranes than micelles.

In collaboration with the group of Martina Huber at the University of Leiden, we have investigated the structure of α-synuclein on SUVs using pulsed EPR techniques[44] that enable the acquisition of long-range information on the conformation of α-synuclein bound to the vesicle surface. In short, the distances between pairs of spin labels introduced by site-selective cysteine mutagenesis were measured for four double-cysteine mutants, α-synuclein-9/90, α-synuclein-18/90, α-synuclein-18/69, and α-synuclein-9/69, each containing one

label in the proposed helix 1, and a second label in helix 2 (see Figure 4). These cysteine residues were labeled with MTSL (1-oxy-2,2,5,5 tetramethylpyrroline-3-methyl-methanethiosulfonate). EPR measurements on labeled α-synuclein in the presence of SUVs of POPG [1-palmitoyl-2-oleoyl-*sn*-glycero-3-(phosphorac-(1-glycerol))] lipids yielded distance distributions that provided a redundant set of distances that proves that the arrangement of the two helices must be antiparallel, as shown in Figure 4. This result has implications for the conformation of α-synuclein *in vivo*, where α-synuclein interacts with synaptic vesicles with diameters of around 40 nm.

## 2.219.3. Aggregation Intermediates

### 2.219.3.1. Aggregation Kinetics

The development of cross-β conformation during amyloid formation is commonly detected by the interaction with specific *fluorescent dyes*, such as Congo red and thioflavin T. The most frequently used dye, thioflavin T, shows significantly enhanced fluorescence emission upon binding to cross-β conformations,[58–60] and is therefore a very useful dye to follow the kinetics of amyloid formation. In general, *in vitro* kinetics studies utilize purified, often recombinantly produced, proteins that spontaneously form amyloid fibrils when incubated at specific conditions of protein concentration, temperature, pH, ion concentration, and agitation.

The formation of amyloid fibrils usually involves a lag phase, during which a sufficient concentration of nucleating species is formed to initiate the subsequent rapid development of protofilaments, protofibrils, and mature fibrils. Elimination of the lag phase can be accomplished by seeding; the addition of a small amount of preassembled fibrils to monomers induces the start of amyloid formation almost instantaneously. Considering disease-related amyloid formation, it is important to note that during the lag phase, oligomers are formed that have been hypothesized to be the potentially toxic species.[61–63] Figure 6 illustrates the difference in aggregation kinetics for an unseeded and a seeded aggregation reaction of recombinantly produced α-synuclein performed with constant shaking. For the unseeded aggregation, the thioflavin T fluorescence intensity curve clearly displays a lag phase, followed by a phase of rapid growth and the saturated final stage. Upon seeding, the thioflavin T emission intensity increases right from the beginning.

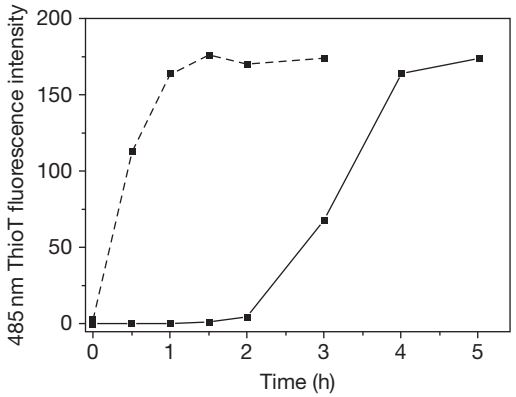


**Figure 6** Aggregation of α-synuclein followed in time by thioflavin T fluorescence. Solid line: without seeding; dashed line: with seeding.

Thioflavin T is a popular and useful dye to follow the kinetics of amyloid fibril formation, although the binding is rather unspecific and the sensitivity quite poor. Especially in the lag phase, where processes from dimerization to oligomerization take place, thioflavin T is not sufficiently sensitive to resolve these important stages. Therefore, in search for better alternatives, novel dyes have been developed and synthesized that are promising specifically for detection of early stage aggregates.[64–68]

### 2.219.3.2. Morphology of Aggregation Intermediates

Aggregation intermediates of amyloidogenic proteins have characteristic dimensions in the nanometer range, which makes them ideally suited for study by *AFM*. AFM[69] is a scanning probe microscopy technique derived from scanning tunneling microscopy (STM) (**Chapter 3.302, Atomic Force Microscopy**). In AFM, a cantilever with a sharp (typically 10 nm) tip scans across a surface and records topography and material properties of the sample surface through the variation in tip–sample interaction forces experienced by the cantilever. Specifically for imaging of relatively soft biological samples such as DNA, proteins, and cells, and also for amyloid fibrils, the AFM technique has several advantages over scanning electron microscopy (SEM): no special sample treatment is required; measurements can be performed in ambient air and in physiologically relevant aqueous milieus without a need for a vacuum environment;[70,71] and measurement of true heights in the nanometer range is possible. The application of AFM to biological and supramolecular systems has been reviewed in recent publications.[70–74] In amyloid fibril research, AFM can be used as an imaging modality, mapping the topography and material properties of the protein aggregates, and also for force spectroscopy measurements, where the tip is used to push and pull individual protein molecules, dimers, or (proto-) fibrils in a controlled fashion.

The high-resolution AFM technique can be effectively employed to study the aggregation kinetics by imaging the intermediate structures formed after different incubation times[75] or by time-lapse imaging of *in situ* growing fibrils[76] on a surface. Figure 7 gives representative AFM images taken during the α-synuclein aggregation presented in Figure 6 by thioflavin T fluorescence. The early phase images from the unseeded aggregation are dominated by small dot-like aggregates that represent oligomeric structures.

The oligomeric species form a focal point of attention in the field of amyloid fibril formation, because of their proposed toxic function. In the course of the aggregation, the oligomeric species is replaced by an increasing number of fibrils. The AFM images demonstrate that thioflavin T is indeed not suitable as an early indicator of amyloid formation; after 90 min, the thioflavin T emission intensity of the unseeded aggregation reaction is still at background level, while the AFM images already show some fibrils.

Because of its exceptionally high spatial resolution, the AFM technique is applicable not only for kinetic studies but also for

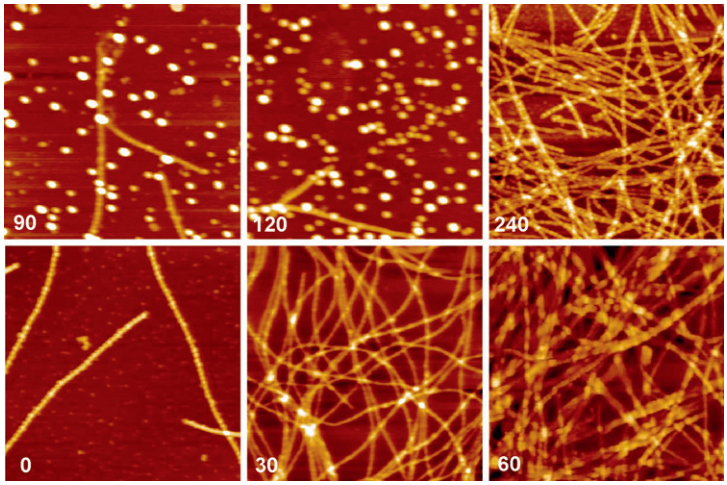


**Figure 7** AFM images taken at different time points, indicated in hours, during aggregation of α-synuclein. Top row unseeded aggregation; bottom row seeded aggregation. Image size: 2.5 × 2.5 μm. Height scale: 10 nm.

quantitative morphological analysis of the fibrillar aggregation products formed (see Section 2.219.4.1).

### 2.219.3.3. Secondary Structure of Aggregation Intermediates

*CD spectroscopy* is an attractive method to monitor conformational changes and transitions in the course of the amyloid formation process[77] (see also Section 2.219.2.1). Figure 8 shows far-UV CD spectra measured from monomeric and oligomeric (lag phase) α-synuclein indicating random-coil and β-sheet structure, respectively. The CD spectrum of monomeric α-synuclein shows a minimum at 198 nm and close to zero CD signals in the 210–220 nm region, which is characteristic for an unfolded protein. The spectrum of the oligomers is completely different, and with a minimum at 220 nm typical for β-sheet structure. Specifically, in the early aggregation phase, where thioflavin T is not sufficiently sensitive, CD spectroscopy is able to demonstrate changes in protein conformation.

Alternatively, *Raman spectroscopy*[78–80] is another method that may be applied to obtain information on the secondary structure content of aggregation intermediates (Chapter 3.322, Infrared and Raman Microscopy and Imaging of Biomaterials).

### 2.219.3.4. Protein Interactions

In a natural *in vivo* environment, amyloid formation takes place in the presence of many other components. Interactions with various chemical and biological components such as metal ions, proteins, and enzymes, are therefore likely. In this context, we have studied the interaction of the enzyme tissue transglutaminase (tTG) with α-synuclein protein variants at physiologically relevant concentrations. The tTG enzyme catalyzes cross-link formation between protein-bound glutamine residues and primary amines and plays a role in various neurodegenerative diseases.[81] tTG enzyme activity has been shown to be upregulated in PD affected brain.[82] tTG-catalyzed cross-links have been found colocalized with Lewy bodies, the cytoplasmic inclusions composed of fibrillar α-synuclein that are characteristic of PD,[11] suggesting a role for tTG in the

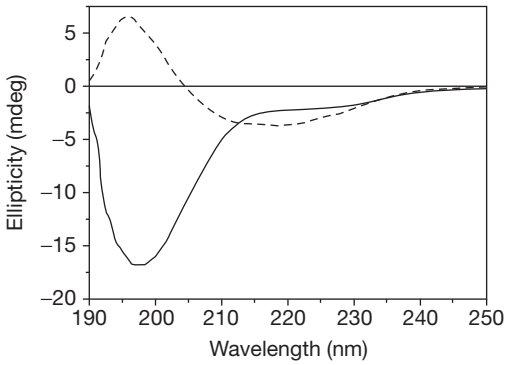


**Figure 8** CD spectra of monomeric (solid line) and oligomeric (dashed line) α-synuclein.

pathophysiology of PD.[83] Cross-linked α-synuclein appeared to correlate with disease progression, indicating that tTG cross-linking may change the structure of monomeric α-synuclein resulting in altered functionality. Intramolecular cross-linking by tTG was hypothesized to be protective in PD, by inhibiting the assembly of monomeric α-synuclein into amyloid fibrils and its potentially toxic oligomeric precursors.[84]

To shed light on the pathological relevance of tTG cross-linking, we have systematically investigated tTG cross-linking of wild-type and disease-related mutant A30P, E46K, and A53T α-synuclein.[85] We evaluated the effect of physiologically relevant[86,87] nanomolar tTG concentrations on cross-linking kinetics, on affected α-synuclein fraction, and on inhibition of aggregation.

Figure 9(a) shows that nanomolar tTG concentrations are sufficient for complete inhibition of fibrillization by effective α-synuclein cross-linking, resulting predominantly in intramolecularly cross-linked monomers accompanied by an oligomeric fraction. AFM indicated the formation of very distinct, uniform, oligomeric species (Figure 9(b)). As oligomeric α-synuclein structures are most likely implicated in the pathophysiology of PD,[84] we determined the secondary structure, foldability, and vesicle permeabilization properties of

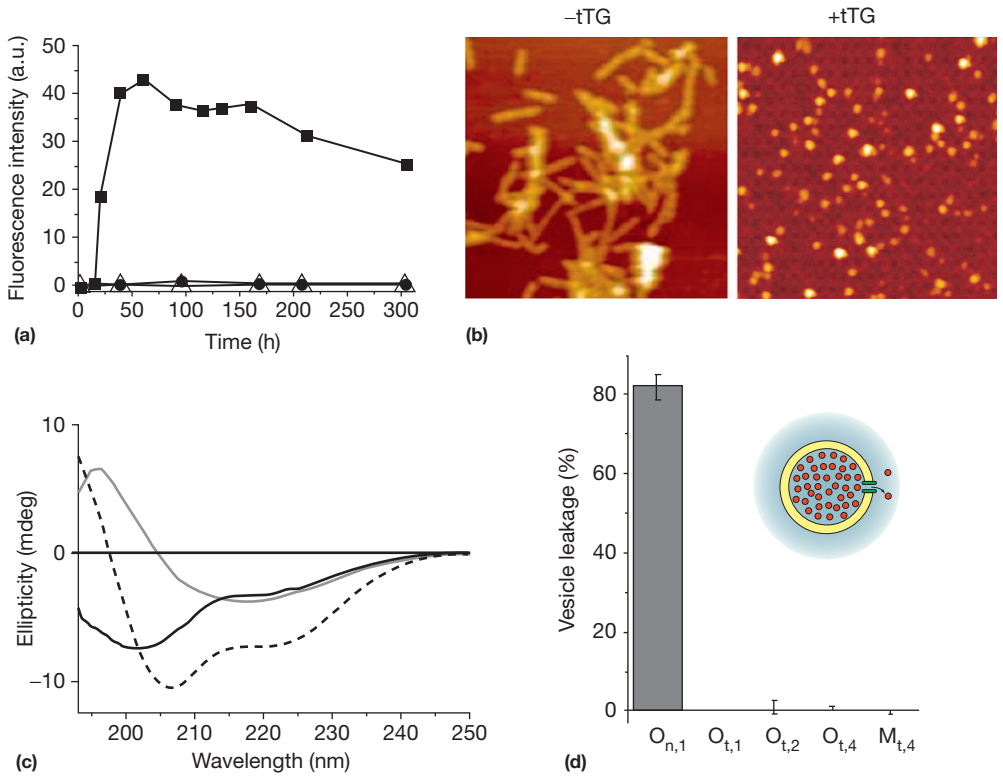


**Figure 9** Aggregation of 100 μM E46K α-synuclein in the presence and absence of tTG. (a) Thioflavin T fluorescence assay: without (squares), and with 50 nM (circles) and 1.3 μM tTG (triangles). (b) AFM images: after 214 h without tTG (left) and after 310 h with 1.3 μM tTG. Images are $1.25 \times 1.25\ \mu m^2$. (c) CD spectra of tTG/α-synuclein oligomers and normal α-synuclein oligomers. Black spectra: oligomeric tTG/α-synuclein, before (solid line) and after (dashed line) addition of 0.1% (w/v) SDS. Gray spectrum: normal α-synuclein oligomers. (d) Vesicle permeabilization assay. $O_{n,1}$: normal α-synuclein oligomers used at 1 μM; $O_{t,1}$, $O_{t,2}$, and $O_{t,4}$: tTG/α-synuclein oligomers used at 1, 2, and 4 μM, respectively. $M_{t,4}$: tTG/α-synuclein monomers used at 4 μM.

purified tTG/α-synuclein oligomers compared to normal oligomers. Our results demonstrate that although tTG/α-synuclein oligomers contain no secondary structure (Figure 9(c)), they are nevertheless able to fold into α-helix conformation on binding SDS. To investigate the membrane permeabilization capability of the tTG/α-synuclein oligomers, we performed a dye efflux assay.[88] POPG LUVs were prepared by drying an aliquot of a solution in chloroform. After rehydration in a buffer solution containing the fluorescent dye calcein, the solution was extruded through a 100 nm pore size polycarbonate membrane filter. Free dye was removed by gel filtration and the phospholipid concentration of the calcein-filled LUVs was determined.[89] In the permeabilization assay, 40 μM phospholipid-containing vesicle solution was mixed 1:1 (v/v) with α-synuclein solution and incubated for 30 min at room temperature. Fluorescence (emission: 505–550 nm, excitation: 494 nm) was measured using a spectrofluorimeter. From the background-corrected fluorescence, the vesicle leakage was calculated relative to maximum vesicle disruption induced by 0.5% (w/v) Triton X-100. Figure 9(d) indicates that the tTG/α-synuclein oligomers, unlike normal oligomers, are not capable of permeabilizing phospholipid vesicles.

The comprehensive data that we have acquired suggest that tTG binds to all α-synuclein variants effectively and prevents formation of toxic oligomers and successive progression into fibrils by forming intramolecular cross-links, imposing structural constraints on α-synuclein. The formation of small, harmless, tTG cross-linked, α-synuclein assemblies suitable for removal by intracellular degradation systems may be a mechanism to prevent formation of pathogenic aggregates. We speculate that intramolecular cross-linking may be the predominant process early in PD, while at later stages, with higher tTG and α-synuclein concentrations[81,90] the probability of intermolecular cross-linking and formation of large, insoluble protein clusters may increase.

## 2.219.4. Mature Amyloid Fibrils

### 2.219.4.1. Structural Polymorphism of Amyloid Fibrils

The structural polymorphism of amyloid fibrils, resulting in a multitude of distinct morphologies, is a particularly important element in scientific understanding of amyloid fibrillogenesis[91] because polymorphism suggests that it is likely that there are multiple pathways of amyloid fibril formation and potential neurodamage. Particularly in this area, nanoscale imaging methods such as AFM can contribute to the understanding of amyloid fibril formation. From high-resolution AFM images, the multitude of aggregate morphologies that occur both *in vivo* and *in vitro* may be classified. In general, amyloid fibrils are unbranched, linear fibrils with a diameter of around 10 nm and lengths that run into the micrometer range.

The discovery by AFM imaging of several types of filaments differing in their diameter, and the observation of periodicity or even twist in the thicker fibrils, has led to the development of the hierarchical assembly model (HAM).[59] This model describes that mature fibrils consist of a twisted pair of protofibrils, each of which is composed of two thinner intertwined protofilaments. However, polymorphism observed by AFM and scanning transmission electron microscopy in amyloid-β (Aβ) fibrils suggests that other mechanisms, not involving protofilaments, may also play a role in the assembly of amyloid fibrils.[92] Possibly mature fibrils are also formed by assembly of discrete independent entities, morphologically resembling twisted fibrils.

Mature fibrils formed by various proteins differ in the number of constituent filaments. For example, $\beta_2$-microglobulin fibrils, involved in dialysis-related amyloidosis, form three types of mature fibrils: consisting of two or four intertwined filaments, or consisting of four filaments and forming a twisted-ribbon structure.[93] These authors also found fibrils exhibiting supercoiling: the superhelical twist period was twice the twist period, which gives the fibrils a zig-zag appearance. Whether the various species form sequentially or in parallel is as yet unclear.

Polymorphism is evident not only when comparing different fibrils. Fibrils formed by full-length prion protein display polymorphism even within individual fibrils, differing in number of constituent filaments and twisting at different points along their length.[22,23] One assembly mechanism that may contribute to this behavior is 'lateral seeding': monomers and oligomers from solution may attach to an existing fibril surface and initiate a new filament alongside an existing filament. This mechanism has been proposed for insulin,[94] when fibrils were formed at an unusual condition of high pressure. However, an argument against the generality of lateral seeding is that the mechanism implies that fibrils would grow in width indefinitely, whereas it has been shown on fibrils formed by many different proteins and peptides that only a small range of fibril diameters is formed.

We have used different contrast modes of high-resolution AFM to study in detail the morphology of α-synuclein fibrils prepared *in vitro* from recombinantly produced wild-type human α-synuclein and the familial disease-related A30P, E46K, and A53T mutant proteins.[95] Aggregation half-times measured using thioflavin T fluorescence spectroscopy at low salt reaction conditions indicated different aggregation kinetics for the variants: 150 h for wild-type and 75, 100, and 250 h for A53T, E46K, and A30P, respectively. These results are consistent with the literature.[96] AFM images in air (**Figure 10(a)–10(d)**) were recorded to verify if the different aggregation kinetics influence the fibril morphologies. Visual inspection of the images suggests that the morphology is not identical for all variants.

Quantitative analysis was performed of heights, modulation depths, and periodicities of a large number of fibrils for each variant (**Figure 10(e)** and **10(f)** and **Table 1**).[97] Wild-type fibrils exhibit the lowest height; A30P and E46K have intermediate values, while A53T fibrils are highest. The modulation depth is not significantly different among the mutant proteins, although wild-type protein has a smaller modulation depth commensurate with the lower measured fibril height. Together with the fibril height, the periodicity of the fibrils is the most characteristic parameter for each α-synuclein variant. The E46K mutant displays a very distinct average periodicity of about 60 nm, A53T an intermediate value of 110 nm, and wild-type and A30P display the largest periodicities of ~140 nm. The distribution of period lengths is narrowest for E46K (main mode at 40–50 nm), whereas A30P and A53T display wider distributions. Wild-type protein displays a main

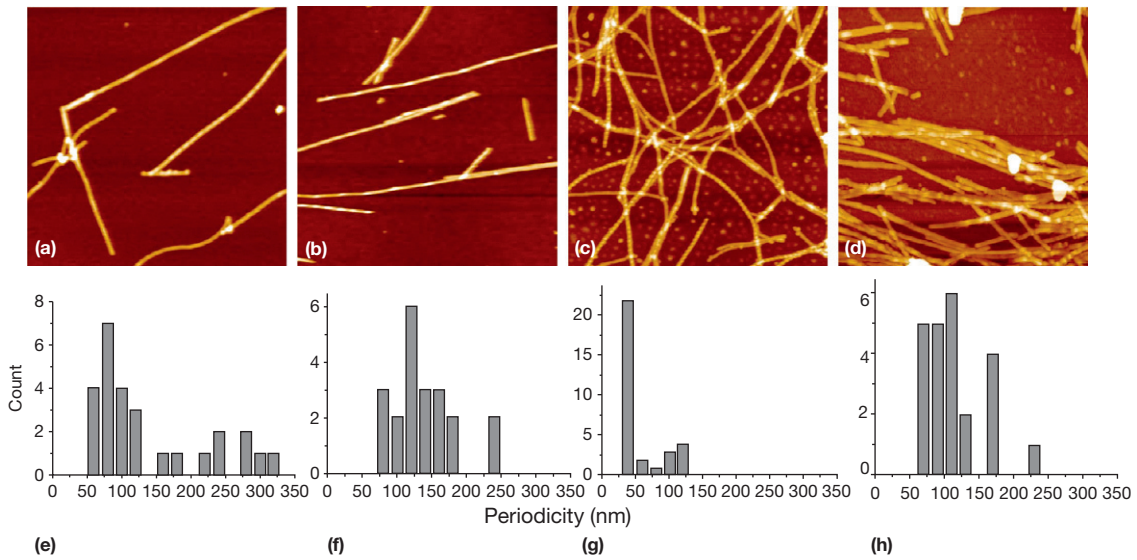


**Figure 10** Representative tapping mode AFM images of wild-type (a), A30P (b), E46K (c), and A53T (d) variants of α-synuclein in air. The color scale represents 15.6 nm in height for wild-type, 20.2 nm for A30P, 22.4 nm for E46K, and 31.3 nm for A53T α-synuclein. Image size is 2500 × 2500 nm. Distributions of fibril periodicities are given for wild-type (e), A30P (f), E46K (g), and A53T (h) variants of α-synuclein. The number of fibrils analyzed is indicated in **Table 1**. Histogram bin size is 20 nm.

periodicity of around 80 nm, but larger periodicities were also observed. The fibril heights and modulation depths measured in air for A30P and E46K variants are consistent, within the accuracy of the data, with earlier AFM results in liquid.[97] The measured heights and modulation depths of wild-type protein are somewhat smaller in air than in liquid. Periodicities measured for A30P and E46K are similar in air and in liquid, and also for wild-type protein considering the main mode in the broad distribution.

Table 1 summarizes the quantitative data obtained and indicates that a single-point mutation in the α-synuclein protein has significant consequences for the ultrastructure of the fibrils formed.

High-resolution phase images were recorded to examine the nanoscale structure of individual α-synuclein fibrils in detail. Phase imaging is sensitive to differences in material properties like sample viscoelasticity or hydrophobicity, and is a complementary contrast mode yielding more details than can be observed in height images.[98] Fibrils shown in Figure 11(a) clearly display twisted fibril morphology, providing evidence for the presence of a skewed pitch. In contrast, Figure 11(b) shows a high-resolution image of a small area scan revealing assembly of fibril segments of 100–150 nm in length. Figure 11(c) and 11(d) demonstrate that both assembly modes can be found within one sample, an observation made for all α-synuclein variants.

Our results indicate that the aggregation of genetic variants of α-synuclein not only follows different kinetics but is also accompanied by the formation of morphologically different fibrils. Individual mutant forms of α-synuclein fibrils may be distinguished on the basis of their characteristic heights and periodicities. Specific point mutations appear to affect fibril assembly and may drive fibril formation into energetically more favorable structures with characteristic periodicity. The measured modulation depths in relation to the fibril heights are compatible with a twisted HAM within the accuracy of the data. For this model, we expect the modulation depth not to exceed 25% of the maximum height of the fibril, an expectation supported by the data shown in Table 1. However, we also observe morphologies that do not resemble the expected twisted structure, but appear like a series of associated segments. This type of morphology has also been observed for insulin fibrils.[94] We thus have evidence for both hierarchical and segmented α-synuclein fibril formation, potentially on the basis of a multipathway mechanism. We speculate that segmented assembly may precede the twist formation, because we mainly observe segmented morphologies in lower height fibrils (protofibrils). Higher resolution imaging and further analysis are required for definitive conclusions.

*Tapping mode AFM* (TM-AFM) *phase imaging* provides another unique source of information on the mechanical properties of amyloid fibrils.[99] The contrast mechanism in TM-AFM phase contrast imaging is the time lag between the oscillation of the cantilever and the driving oscillation. This lag is due to the interaction between the tip and the sample/substrate, which may depend on any number of material properties and the electrical charge of tip and sample. For good phase contrast imaging, the correct choice of tapping frequency, tapping amplitude, set-point ratio, humidity, the thickness of a potential thin water layer on the dry sample, and surface charges on the tip and/or the sample are important. We have recently obtained high-resolution AFM phase contrast images (Figure 12) that demonstrate that the ends of the α-synuclein fibrils and certain specific points in the bulk of the fibrils have a decidedly different phase lag than the rest of the fibril, possibly representing local differences in material properties. The resolution of these patches of alternate tip–sample interaction is higher than the resolution of the height image, presumably because only just the 'tip of the tip' participates in the interactions that cause the phase difference. Possibly for the same reason, tip–sample convolution does not reduce the phase resolution in the same way as it reduces the lateral resolution

**Table 1** Quantitative characteristics of fibrils of α-synuclein variants

| *α-synuclein variant* | *N fibrils* | *Fibril top height (nm)* | *Modulation depth (nm)* | *Periodicity (nm)* |
|---|---|---|---|---|
| Wild-type | 33 (27) | $7.5 \pm 0.9$ | $1.5 \pm 0.4$ | $141 \pm 82$ |
| A30P | 41 (21) | $8.7 \pm 1.4$ | $2.3 \pm 0.7$ | $139 \pm 46$ |
| E46K | 37 (29) | $9.8 \pm 1.2$ | $2.1 \pm 0.6$ | $59 \pm 28$ |
| A53T | 33 (20) | $10.4 \pm 1.3$ | $2.2 \pm 0.8$ | $115 \pm 41$ |

*N fibrils* is the total number of fibrils analyzed per mutant; the number of periodic fibrils is in brackets. The fibrils classified as nonperiodic were irregular in height. Height values are averages over all *N* fibrils; the modulation depth and periodicity are calculated over only the periodic fibrils. The standard deviation is used as the measurement error.

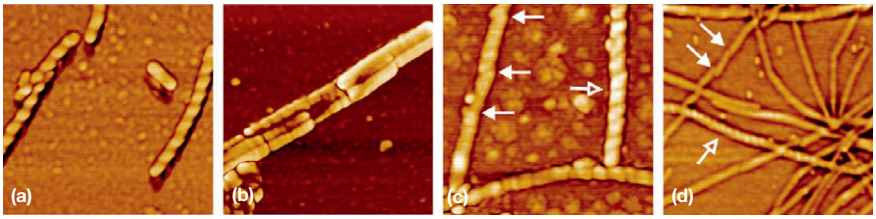


**Figure 11** Tapping mode AFM phase images in air. (a) E46K fibrils displaying twisted morphology. (b) Wild-type fibril with appearance of associated segments. (c) and (d) Contain both twisted and segmented E46K fibrils. Image sizes are for (a), (b), and (c): $620 \times 620$ nm, for (d) $1250 \times 1250$ nm. Closed arrows point out segmented fibrils, open arrows twisted fibrils.

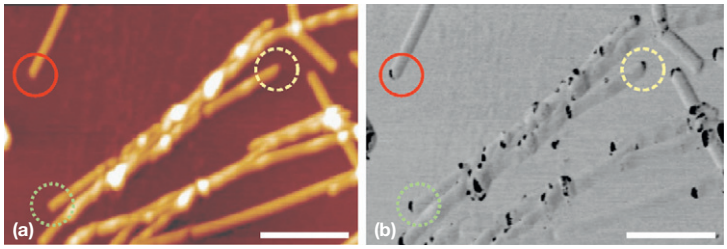


**Figure 12** AFM phase contrast shows high-resolution fibril features TM-AFM height image of α-synuclein fibrils (a) with the corresponding simultaneously recorded AFM phase contrast image (b). The phase image (b) shows that fibril ends (*circles*) and certain specific parts of the fibril bulk have material properties different from those of the bulk fibril. Scale bar 500 nm, resolution 256 pixels/line.

of height images. The exact origin of the oscillation lag and thus of the phase contrast is unclear, but probably involves the higher harmonic mode of the cantilever oscillation as the tapping cantilever touches the sample surface.

The examples given here indicate that phase contrast imaging holds great promise as a method for characterization of material properties of amyloid fibrils. Phase imaging may play an important role in providing the necessary differential contrast and sensitivity that are lacking in height images to reveal differences in material properties at fibril segment interfaces.

### 2.219.4.2. Mechanical Deformation of Fibrils

The application of AFM imaging is not limited to characterization of fibril morphology properties under various conditions by imaging; also the mechanical properties of the fibrils may be deduced from the images. In contact mode AFM (CM-AFM), the tip is in constant contact with the surface. The tip is effectively 'dragged along' the sample while the feedback loop keeps the interaction force constant by maintaining the deflection at a set-point value. This mode allows for very high lateral resolution on periodic samples with low corrugation, but is typically too damaging for fibrillar protein aggregates, especially in liquid. The damaging nature of CM-AFM can be used as a tool to study the effect of controlled damage applied to fibrillar aggregates. Figure 13(a) depicts an image of A30P mutant fibrils obtained by scanning in tapping mode. Then the same area was rescanned in contact mode, followed by another larger scan in tapping mode. The combined images taken before and after contact mode scanning clearly show deformed fibrils in the area scanned in contact mode; outside this area the fibrils are not affected. The regular pattern of nanoscale deformations is the result of the force imposed on the fibrils during contact mode scanning (Figure 13(b)). A closer look at a single fibril reveals that the spacing between the deformations corresponds to the 140 nm periodicity of the original intact fibrils (Figure 13(c) and 13(d)). Figure 13 shows that α-synuclein fibrils have 'weak spots' at intervals corresponding to their periodicity.[95,97] This same effect was found for Aβ: N-terminal 1–42 residues ($A\beta_{1\text{-}42}$) fibrils.[100] Fibrils may be damaged by indentation forces ranging from 40 to 100 nN.[101,102]

Lateral forces in contact mode are much higher than in tapping mode because the tip is continuously in contact with the sample. The contact force is mainly dominated by the adhesion force between the $Si_3N_4$ tip and the sample. The periodicity of the deformations may arise from the

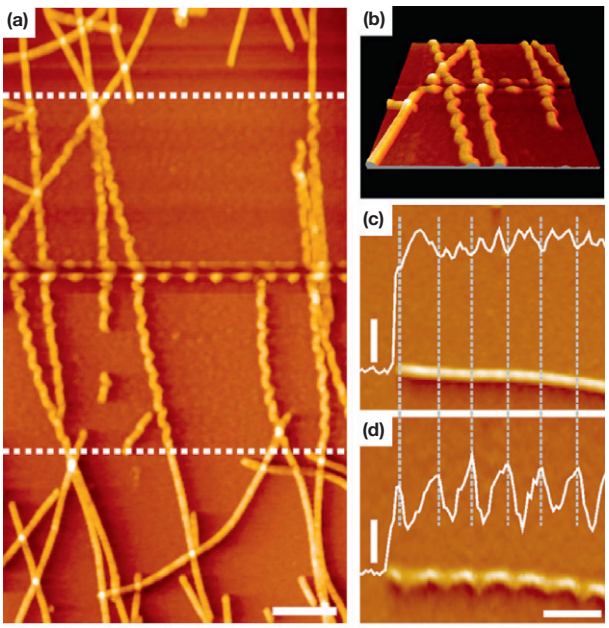


**Figure 13** Contact mode AFM imaging reveals mechanical weak spots in α-synuclein fibrils. (a) Composite tapping mode AFM height image of A30P α-synuclein fibrils. The section between the *dotted lines* has been subjected to contact mode imaging before this image was made. The horizontal track in the middle results from repeated line scanning for optimization of imaging parameters. Scale bar 500 nm. (b) 3D rendering of affected area. Comparison of morphology of one fibril before (c) and after (d) contact mode imaging. The height profiles show that least damage was done on those sections that were lowest before scanning (*gray dashed lines*, scan direction was vertical). Horizontal scale bar 200 nm, vertical scale bars 2 nm.

characteristic fibril structure, assembled in such a way that it is locally more sensitive to deformation by lateral force. Another reason may be the intrinsic variation in adhesion force. Hydrophilic parts of the sample will display higher adhesion forces.[103] Possibly, these fibril parts are more prone to damage by high local lateral forces. The fibril deformation results may support both hierarchical and segmented α-synuclein fibril assembly. This AFM-based fibril deformation method may be applied more generally to study the mechanical properties of various fibrillar structures. The extent of the deformations may be even converted into quantitative mechanical data.

## 2.219.5. Conclusion

Amyloids experience a growing scientific interest, from both a fundamental biomedical and a materials science perspective. Initially amyloid formation was observed as a pathological hallmark of several neurodegenerative diseases. More recently functional amyloids have been discovered in many species, and these structures also play a role in industrial processes, such as in the optimization of food texture. Nevertheless, the process of amyloid formation is still not well understood. More knowledge about the mechanism and about factors that may affect fibril formation will improve our understanding of the molecular origin of amyloid diseases and about the role of functional amyloid. In the case of pathogenic amyloid, this information is indispensable in the search for effective medication, when targeting of a specific aggregation stage may be considered. Widespread application and exploitation of amyloid nanobiomaterials require further information about not only the details of the aggregation process, but also the final material properties.

This chapter describes the application of a variety of biophysical approaches to understand important aspects of amyloid fibril formation. Although we have mainly focused on a single model system, the human α-synuclein protein, the approaches are generally applicable to the broader genre of amyloid-forming proteins.

## Acknowledgments

The authors thank Kees van der Werf for assistance and advice on atomic force microscopy; Kirsten van Leijenhorst-Groener, Yvonne Kraan, and Marloes ten Haaff-Kolkman are acknowledged for production and purification of α-synuclein protein. We acknowledge a fruitful collaboration with Martina Huber at Leiden University, and Malte Drescher at the University of Konstanz for the EPR work. The described work is part of the research program of the 'Stichting voor Fundamenteel Onderzoek der Materie (FOM),' which is financially supported by the 'Nederlandse Organisatie voor Wetenschappelijk Onderzoek (NWO).' Financial support is also provided by the Stichting Internationaal Parkinson Fonds, Hoofddorp, The Netherlands.

## References

1. Dobson, C. M. *Nature* **2003**, *426*, 884–890.
2. Otzen, D.; Nielsen, P. H. *Cell. Mol. Life Sci.* **2008**, *65*, 910–927.
3. Fowler, D. M.; Koulov, A. V.; Balch, W. E.; Kelly, J. W. *Trends Biochem. Sci.* **2007**, *32*, 217–224.
4. Fowler, D. M.; Koulov, A. V.; Alory-Jost, C.; Marks, M. S.; Balch, W. E.; Kelly, J. W. *PLoS Biol.* **2006**, *4*, 100–107.
5. Pearce, F. G.; Mackintosh, S. H.; Gerrard, J. A. *J. Agric. Food Chem.* **2007**, *55*, 318–322.
6. Gras, S. L.; Squires, A. M.; Dobson, C. M.; MacPhee, C. E. Functionalised fibrils for bio-nanotechnology. In *Proceedings of the 2006 International Conference on Nanoscience and Nanotechnology*, ICONN, South Korea, 2006; Vols. 1 and 2 265–267.
7. Wang, C.; Hunag, L.; Wang, L.; Hong, Y.; Sha, Y. *Biopolymers* **2007**, *86*, 23–31.
8. Malisauskas, M.; Meskys, R.; Morozova-Roche, L. A. *Biotechnol. Prog.* **2008**, *24*, 1166–1170.
9. Rambaran, R. N.; Serpell, L. C. *Prion* **2008**, *2*, 112–117.
10. Goedert, M. *Nat. Rev. Neurosci.* **2001**, *2*, 492–501.
11. Spillantini, M. G.; Schmidt, M. L.; Lee, V. M.-Y.; Trojanowski, J. Q.; Jakes, R.; Goedert, M. *Nature* **1997**, *388*, 839–840.
12. Tompa, P. *Structure and Function of Intrinsically Disordered Proteins*; CRC Press: Boca Raton, FL, 2010.
13. Chiti, F.; Dobson, C. M. *Annu. Rev. Biochem.* **2006**, *75*, 333–366.
14. Buxbaum, J. N. *Trends Biochem. Sci.* **2003**, *28*, 585–592.
15. Selkoe, D. J. *Nature* **2003**, *426*, 900–904.
16. Soto, C. *Nat. Rev. Neurosci.* **2003**, *4*, 49–60.
17. Shults, C. W. *Proc. Natl Acad. Sci. USA* **2006**, *103*, 1661–1668.
18. Spillantini, M. G.; Crowther, R. A.; Jakes, R.; Hasegawa, M.; Goedert, M. *Proc. Natl Acad. Sci. USA* **1998**, *95*, 6469–6473.
19. Krüger, R.; Kuhn, W.; Müller, T.; *et al. Nat. Genet.* **1998**, *18*, 106–108.
20. Polymeropoulos, M. H.; Lavedan, C.; Leroy, E.; *et al. Science* **1997**, *276*, 2045–2047.
21. Zarranz, J. J.; Alegre, J.; Gómez-Esteban, J. C.; *et al. Ann. Neurol.* **2004**, *55*, 164–173.
22. Anderson, M.; Bocharova, O. V.; Makarava, N.; Breydo, L.; Salnikov, V. V.; Baskakov, I. V. *J. Mol. Biol.* **2006**, *358*, 580–596.
23. Anderson, J. P.; Walker, D. E.; Goldstein, J. M.; *et al. J. Biol. Chem.* **2006**, *281*, 29739–29752.
24. Chen, L.; Feany, M. B. *Nat. Neurosci.* **2005**, *8*, 657–663.
25. Fujiwara, H.; Hasegawa, M.; Dohmae, N.; *et al. Nat. Cell Biol.* **2002**, *4*, 160–164.
26. Okochi, M.; Walter, J.; Koyama, A.; *et al. J. Biol. Chem.* **2000**, *275*, 390–397.
27. Murphy, D. D.; Rueter, S. M.; Trojanowski, J. Q.; Lee, V. M.-Y. *J. Neurosci.* **2000**, *20*, 3214–3220.
28. Chandra, S.; Gallardo, G.; Fernández-Chacón, R.; Schlüter, O. M.; Südhof, T. C. *Cell* **2005**, *123*, 383–396.
29. Weinreb, P. H.; Zhen, W.; Poon, A. W.; Conway, K. A.; Lansbury, P. T., Jr. *Biochemistry* **1996**, *35*, 13709–13715.
30. Davidson, W. S.; Jonas, A.; Clayton, D. F.; George, J. M. *J. Biol. Chem.* **1998**, *273*, 9443–9449.
31. Eliezer, D.; Kutluay, E.; Bussel, R., Jr.; Browne, G. *J. Mol. Biol.* **2001**, *307*, 1061–1073.
32. Serpell, L. C.; Berriman, J.; Jakes, R.; Goedert, M.; Crowther, R. A. *Proc. Natl Acad. Sci. USA* **2000**, *97*, 4897–4902.
33. Gambin, Y.; Schug, A.; Lemke, E. A.; *et al. Proc. Natl Acad. Sci. USA* **2009**, *106*, 10153–10158.
34. Veldhuis, G.; Segers-Nolten, I.; Ferlemann, E.; Subramaniam, V. *Chembiochem* **2009**, *10*, 436–439.
35. Jares-Erijman, E. A.; Jovin, T. M. *Nat. Biotechnol.* **2003**, *21*, 1387–1395.
36. Lakowicz, J. R. *Principles of Fluorescence Spectroscopy*, 2nd ed.; Kluwer Academic/Plenum Publishers: New York, 2002.
37. Wu, P.; Brand, L. *Anal. Biochem.* **1994**, *218*, 1–13.
38. Periasamy, A. *J. Biomed. Opt.* **2001**, *6*, 287–291.
39. dos Remedios, C. G.; Moens, P. D. *J. Struct. Biol.* **1995**, *115*, 175–185.
40. Stryer, L. *Annu. Rev. Biochem.* **1978**, *47*, 819–846.
41. Ulmer, T. S.; Bax, A.; Cole, N. B.; Nussbaum, R. L. *J. Biol. Chem.* **2005**, *280*, 9595–9603.
42. Pelton, J. T.; McLean, L. R. *Anal. Biochem.* **2000**, *277*, 167–176.
43. Ferreon, A. C. M.; Deniz, A. A. *Biochemistry* **2007**, *46*, 4499–4509.
44. Drescher, M.; Veldhuis, G.; van Rooijen, B. D.; Milikisyants, S.; Subramaniam, V.; Huber, M. *J. Am. Chem. Soc.* **2008**, *130*, 7796–7797.
45. Bussell, A., Jr.; Eliezer, D. *J. Biol. Chem.* **2001**, *276*, 45996–46003.
46. Deniz, A. A.; Laurence, T. A.; Beligere, G. S.; *et al. Proc. Natl Acad. Sci. USA* **2000**, *97*, 5179–5184.
47. Merchant, K. A.; Best, R. B.; Louis, J. M.; Gopich, I. V.; Eaton, W. A. *Proc. Natl Acad. Sci. USA* **2007**, *104*, 1528–1533.
48. Mukhopadhyay, S.; Krishnan, R.; Lemke, E. A.; Lindquist, S.; Deniz, A. A. *Proc. Natl Acad. Sci. USA* **2007**, *104*, 2649–2654.
49. Schuler, B.; Eaton, W. A. *Curr. Opin. Struct. Biol.* **2008**, *18*, 16–26.
50. Schuler, B.; Lipman, E. A.; Eaton, W. A. *Nature* **2002**, *419*, 743–747.
51. Bisaglia, M.; Tessari, I.; Pinato, L.; *et al. Biochemistry* **2005**, *44*, 329–339.
52. Bussell, R., Jr.; Eliezer, D. *J. Mol. Biol.* **2003**, *329*, 763–778.
53. Jao, C. C.; Der-Sarkissian, A.; Chen, J.; Langen, R. *Proc. Natl Acad. Sci. USA* **2004**, *101*, 8331–8336.
54. Bussell, R., Jr.; Ramlall, T. F.; Eliezer, D. *Protein Sci.* **2005**, *14*, 862–872.
55. Chandra, S.; Chen, X.; Rizo, J.; Jahn, R.; Südhof, T. C. *J. Biol. Chem.* **2003**, *278*, 15313–15318.
56. Itri, R.; Amaral, L. Q. *J. Phys. Chem.* **1991**, *95*, 423–427.
57. Rhoades, E.; Ramlall, T. F.; Webb, W. W.; Eliezer, D. *Biophys. J.* **2006**, *90*, 4692–4700.

58. Ban, T.; Hamada, D.; Hasegawa, K.; Naiki, H.; Goto, Y. *J. Biol. Chem.* **2003**, *278*, 16462–16465.
59. Khurana, R.; Coleman, C.; Ionescu-Zanetti, C.; *et al. J. Struct. Biol.* **2005**, *151*, 229–238.
60. Krebs, M. R. H.; Bromley, E. H. C.; Donald, A. M. *J. Structur. Biol.* **2005**, *149*, 30–37.
61. Conway, K. A.; Lee, S.-J.; Rochet, J.-C.; Ding, T.; Williamson, R. E.; Lansbury, P. T., Jr. *Proc. Natl Acad. Sci. USA* **2000**, *97*, 571–576.
62. Danzer, K. M.; Haasen, D.; Karow, A. R.; *et al. J. Neurosci.* **2007**, *27*, 9220–9232.
63. Kayed, R.; Head, E.; Thompson, J.; *et al. Science* **2003**, *300*, 486–489.
64. Celej, M. S.; Caarls, W.; Demchenko, A. P.; Jovin, T. M. *Biochemistry* **2009**, *48*, 7465–7472.
65. Celej, M. S.; Jares-Erijman, E. A.; Jovin, T. M. *Biophys. J.* **2008**, *94*, 4867–4879.
66. Volkova, K. D.; Kovalska, V. B.; Balanda, A. O.; *et al. Bioorg. Med. Chem.* **2008**, *16*, 1452–1459.
67. Volkova, K. D.; Kovalska, V. B.; Balanda, A. O.; *et al. J. Biochem. Biophys. Meth.* **2007**, *70*, 727–733.
68. Volkova, K. D.; Kovalska, V. B.; Segers-Nolten, G. M.; Veldhuis, G.; Subramaniam, V.; Yarmoluk, S. M. *Biotech. Histochem.* **2009**, *84*, 55–61.
69. Binnig, G.; Quate, C. F.; Gerber, C. *Phys. Rev. Lett.* **1986**, *56*, 930–933.
70. Cohen, S. R.; Bitler, A. *Curr. Opin. Colloid Interface Sci.* **2008**, *13*, 316–325.
71. Müller, D. J.; Dufrêne, Y. F. *Nat. Nanotechnol.* **2008**, *3*, 261–269.
72. Gaczynska, M.; Osmulski, P. A. *Curr. Opin. Colloid Interface Sci.* **2008**, *13*, 351–367.
73. Gosal, W. S.; Myers, S. L.; Radford, S.; Thomson, N. H. *Protein Pept. Lett.* **2006**, *13*, 261–270.
74. Samori, P. *Chem. Soc. Rev.* **2005**, *34*, 551–561.
75. Dong, M.; Hovgaard, M.; Xu, S.; Otzen, D. E.; Besenbacher, F. *Nanotechnology* **2006**, *17*, 4003–4009.
76. Goldsbury, C.; Kistler, J.; Aebi, U.; Arvinte, T.; Cooper, G. J. S. *J. Mol. Biol.* **1999**, *285*, 33–39.
77. Uversky, V. N.; Li, J.; Fink, A. L. *J. Biol. Chem.* **2001**, *276*, 10737–10744.
78. Apetri, M. M.; Maiti, N. C.; Zagorski, M. G.; Carey, P. R.; Anderson, V. E. *J. Mol. Biol.* **2006**, *355*, 63–71.
79. Maiti, N.; Apetri, M.; Zagorski, M.; Carey, P.; Anderson, V. *J. Am. Chem. Soc.* **2004**, *126*, 2399–2408.
80. Thomas, G. J., Jr. *Annu. Rev. Biophys. Biomol. Struct.* **1999**, *28*, 1–27.
81. Muma, N. A. *J. Neuropathol. Exp. Neurol.* **2007**, *66*, 258–263.
82. Kim, S.-Y.; Grant, P.; Lee, J.-H.; Pant, H. C.; Steinert, P. M. *J. Biol. Chem.* **1999**, *274*, 30715–30721.
83. Junn, E.; Ronchetti, R. D.; Quezado, M. M.; Kim, S.-Y.; Mouradian, M. M. *Proc. Natl Acad. Sci. USA* **2003**, *100*, 2047–2052.
84. Lashuel, H. A.; Petre, B. M.; Wall, J.; *et al. J. Mol. Biol.* **2002**, *322*, 1089–1102.
85. Segers-Nolten, I. M. J.; Wilhelmus, M. M. M.; Veldhuis, G.; van Rooijen, B. D.; Drukarch, B.; Subramaniam, V. *Protein Sci.* **2008**, *17*, 1395–1402.
86. Konno, T.; Morii, T.; Shimizu, H.; Oiki, S.; Ikura, K. *J. Biol. Chem.* **2005**, *280*, 17520–17525.
87. Murtaugh, M. P.; Arend, W. P.; Davies, P. J. A. *J. Exp. Med.* **1984**, *159*, 114–125.
88. van Rooijen, B. D.; Claessens, M. M. A. E.; Subramaniam, V. *Biochim. Biophys. Acta* **2009**, *1788*, 1271–1278.
89. Chen, P. S.; Toribara, T. Y.; Warner, H. *Anal. Chem.* **1956**, *28*, 1756–1758.
90. Rockenstein, E.; Hansen, L. A.; Mallory, M.; Trojanowski, J. Q.; Galasko, D.; Masliah, E. *Brain Res.* **2001**, *914*, 48–56.
91. Kodali, R.; Wetzel, R. *Curr. Opin. Struct. Biol.* **2007**, *17*, 48–57.
92. Goldsbury, C.; Frey, P.; Olivieri, V.; Aebi, U.; Müller, S. A. *J. Mol. Biol.* **2005**, *352*, 282–298.
93. Kad, N. M.; Myers, S. L.; Smith, D. P.; Smith, D. A.; Radford, S. E.; Thomson, N. H. *J. Mol. Biol.* **2003**, *330*, 785–797.
94. Jansen, R.; Dzwolak, W.; Winter, R. *Biophys. J.* **2005**, *88*, 1344–1353.
95. Segers-Nolten, I.; van der Werf, K.; van Raaij, M.; Subramaniam, V. Quantitative characterization of protein nanostructures using atomic force microscopy. In *Conference Proceedings of the 2007 Annual International Conference of the IEEE Engineering in Medicine and Biology Society*, Lyon, France, 2007; Vols. 1–16, 6609–6612.
96. Hoyer, W.; Cherny, D.; Subramaniam, V.; Jovin, T. M. *Biochemistry* **2004**, *43*, 16233–16242.
97. van Raaij, M. E.; Segers-Nolten, I. M. J.; Subramaniam, V. *Biophys. J.* **2006**, *91*, L96–L98.
98. Argaman, M.; Golan, R.; Thomson, N. H.; Hansma, H. G. *Nucleic Acids Res.* **1997**, *25*, 4379–4384.
99. Moreno-Herrero, F.; Pérez, M.; Baró, A. M.; Avila, J. *Biophys. J.* **2004**, *86*, 517–525.
100. Arimon, M.; Díez-Pérez, I.; Kogan, M. J.; *et al. FASEB J.* **2005**, *19*, 1344–1346.
101. Fukuma, T.; Mostaert, A. S.; Jarvis, S. P. *Tribol. Lett.* **2006**, *22*, 233–237.
102. Mesquida, P.; Riener, C. K.; MacPhee, C. E.; McKendry, R. A. *J. Mater. Sci. Mater. Med.* **2007**, *18*, 1325–1331.
103. van Noort, S. J.; van der Werf, K. O.; de Grooth, B. G.; van Hulst, N. F.; Greve, J. *Ultramicroscopy* **1997**, *69*, 117–127.